MTLA 30 (2023) 101829

Contents lists available at ScienceDirect

Materialia

journal homepage: www.elsevier.com/locate/mtla

Building up europium thulium co-doped yttria nanoparticles with electron paramagnetic resonance response by colloidal synthesis

S.C. Santos *, O Rodrigues Jr, L.L. Campos

Instituto de Pesquisas Energeticas e Nucleares – IPEN, Av. Prof. Lineu Prestes 2242, Cidade Universitaria, Sao Paulo, Brazil

ARTICLE INFO

Keywords:
Yttria
Thulium oxide
Europium oxide
Rare earths
EPR
Dosimetry

ABSTRACT

In the radiation dosimetry field the research for new materials is a continuos demand with the aim to provide highly improvement procedures where ionizing radiation is used. Considering this challenge, the present work reports the colloidal synthesis of europium-thulium-co-doped yttria powders (YET) and evaluates the dopants effect on the promotion of EPR response of yttria. The powdered compositions prepared with up to 2at.%Tm and 2at.%Eu (at.%, atomic percentage) were evaluate by XRD, PCS, SEM, and EPR. Based on the results, the proposed synthesis method provided ceramic powders with cubic C-type form and mean particle size (d_{50}) less than 160nm. The most significant EPR dose-response was noticed for the powdered composition prepared with 0.5at.%Tm ($YET_{0.5}$) as irradiated with 5kGy (^{60}Co). These findings are key parameters to advance toward the formation of new materials for radiation dosimetry.

1. Introduction

Practices that use ionizing radiation energy requires high safety systems in order to protect the humans and the environment against detrimental effects of ionizing radiation [1]. In summary, radiation dosimetry [2] has the aim to measure the absorbed radiation dose which is emitted from a source of ionizing radiation. Additionally, the radiation dose is the amount of radiation energy that is deposited in a substance divided by its mass. Radiation dosimetry demands a continuos improvement of materials to offer a highly safety environment in applications as clinical [3], industry [4], food [5], energy [6], and environmental [7].

Yttria (Y_2O_3) which belongs to the rare earth series (from La to Lu, and Sc) [8] is one of the most important rare earth sesquioxides (RE_2O_3) due to its remarkable properties (mechanical, thermal, chemical, and photonic) [9]. Many studies [10–15] have reported the wide range of applicability of yttria in coatings [16], sintering aids [17], catalysts [18], photo-luminescent devices [19], and biomaterials [20]. Govindan et al. [21] noticed that Ce doped Y_2O_3 nanoparticles with average particle size of 40 investigations on the applicability of yttria nm exhibited photon luminescence in blue wavelength region. Wang et al. [22] found out that Nd doped Y_2O_3 nano-sized powders prepared with 2at.%Nd by a microwave-assisted glycine solution combustion method presented the highest fluorescence intensity at 1078.6nm wavelength. Huang et al. [23] reported that La doped Y_2O_3 ceramics with in-line transmittance of 74% at 800nm can be obtained by sintering at 1700°C in vacuum. Nevertheless, there are few investigations into the applicability of yttria in radiation dosimetry.

Electron Paramagnetic Resonance (EPR) [24], which is also known as Electron Spin Resonance (ESR), is a magnetic resonance technique that detects unpaired electrons in paramagnetic substances, which includes free radicals, transition metal ions, and lattice defects. While Nuclear Magnetic Resonance (NMR) [25] measures the nuclear transitions in a sample, EPR detects the transitions of unpaired electrons in a sample by applying magnetic field and microwave power. Most of materials have unpaired electrons, and their formation can be induced by diverse chemical and physical processes, which include ionizing radiation [26]. In addition, free radicals plays an effective role in many processes, thus EPR technique is used in a wide range of research areas as biology [27], chemistry [28], quantum physics [29], medical [30], and materials science [31]. EPR measurement can be performed in seconds, is non-destructive and non-invasive, maintaining the sample in its original condition/characteristics. Even though EPR is a powerful technique to characterize paramagnetic samples, there are few studies on EPR characterization of yttria based materials. Our studies [32–39] might be the few ones on it. Santos et al. [33] observed that using 2at.% of europium improved the EPR dose response of yttria rods in a range of dose from 0.001 up to 50kGy. Santos et al. [38] noticed that

* Corresponding author.
E-mail address: silas.cardoso@alumni.usp.br (S.C. Santos).

https://doi.org/10.1016/j.mtla.2023.101829
Received 19 December 2022; Accepted 18 June 2023
Available online 19 June 2023

Table 1
Description of the YET powdered compositions obtained by colloidal synthesis.

Sample	Structural formula	Y (at. %)	Eu (at. %)	Tm (at. %)	C (g. L^{-1})
$YET_{0.5}$	$Y_{1.975}Eu_{0.020}Tm_{0.005}O_3$	97.5	2.0	0.5	20.00
$YET_{1.0}$	$Y_{1.970}Eu_{0.020}Tm_{0.010}O_3$	97.0		1.0	
$YET_{1.5}$	$Y_{1.965}Eu_{0.020}Tm_{0.015}O_3$	96.5		1.5	
$YET_{2.0}$	$Y_{1.960}Eu_{0.020}Tm_{0.020}O_3$	96.0		2.0	

at.% is atomic percentage; C is the concentration of the stock solution based on $RE(NO_3)_3$ solutions, in which RE is Y, Eu, and Tm.

thulium-yttria nanoparticles prepared with 0.1at.% of thulium exhibited the most remarkable EPR response as a function of dose among all compositions studied.

Considering the promising results achieved recently by the group, the present work goes further with a significant improvement in the EPR response of yttria by using two rare-earth metal ions as dopants. The motivation of this study consists in co-doping yttria with europium and thulium by colloidal synthesis to promote the formation of new electron defects/radicals into its lattice, which in turn can improve the capacity of yttria to keep the energy deposited from ionizing radiation source (dose) and release it proportionally to the applied dose as stimulated. The results reported in this study are substantial parameters to advance toward formation of new materials for radiation dosimetry.

2. Experimental

2.1. Starting materials

In the present study europium thulium co-doped yttria powders (YET) with controlled characteristics such as chemical stoichiometry, shape, size, surface area, and density were synthesized by using the following starting materials: yttria (Y_2O_3, 99.99%, Alfa Aesar GmbH), thulium oxide (Tm_2O_3, 99.999%, Alfa Aesar GmbH), europium oxide (Eu_2O_3, 99.999%, Alfa Aesar GmbH), nitric acid (HNO_3, Synth), ammonium hydroxide (NH_4OH, Casa Americana), and ethanol (CH_3CH_2OH, Labsynth).

2.2. Synthesis of the YET powders

The formation of the YET nano-sized powders was performed by hydrothermal synthesis, in which the content of the rare-earth dopant was estimated in atomic percentage (at.%) by stoichiometry calculations, and considering yttria as a host reference. The YET compositions were formed by varying thulium content from 0.5at.% up to 2.0at%, while europium content was fixed at 2.0at% (Table 1). The precursor powders (P_{YET}) were obtained by processing a stock solution at 60ºC for 6h in a condenser system, followed by a washing cycle using deionized water as illustrated in Fig. 1 steps 1-5. Finally, the nano-sized powders were formed by thermal treatment up to 1500ºC for 2h in air atmosphere using a box furnace (Lindberg Blue, Haake) as shown in Fig. 1 steps 5 and 6.

2.3. Powder characterization

The aim of performing an evaluation of thermal decomposition of P_{YET} powders was to define a compatible thermal treatment condition to obtain YET particles in a crystalline form. Using a box furnace (Lindberg Blue, Haake) a P_{YET} sample of 5mg was heated from 25ºC up to 1400ºC in air atmosphere, where its mass was measured in each 100ºC, using an analytical balance (Mettler Toledo, AB204-S). In this form, a relationship curve between mass loss (m, mg) and temperature (T,°C) was established. Besides, the first derivate of the mass loss curve as a function of temperature was calculated to determine the temperature at which the maximum decomposition of sample occurred. Therefore, the conditions of thermal treatment of P_{YET} powders to form YET crystalline based materials were proposed taking in account the results achieved during this assay.

The evolution of crystalline structure of the YET powders as a function of the thermal treatment temperature was observed by X-ray diffraction (XRD, Rigaku Multiflex, Japan), considering an angular range (2θ) from 15 to 70º, step size of 0.5º.min^{-1}, and Kα source. The identification of the crystalline phases, Rietveld structure refinement, the mean crystallite size (d_c) expressed in Eq.1, and including electron density distribution of the powdered samples. The electron density distribution is a method of characterization to evaluate the density of electrons in the unit cell of a sample, based on the maximum entropy method (MEM) [40] and performed by PROFEX [41] software. In addition, ball-and-stick and polyhedral representations of the unit cell of a YET composition were drawn by using Vesta [42] software and from MEM method.

$$d_c = \frac{4}{3\pi b_1}\left[\frac{1+2\sqrt{k_1}}{\left(1+\sqrt{k_1}\right)^2}\right][nm] \quad (1)$$

Where b_1 is peak width and k_1 is structure file parameter. Additionally, the relationship of these parameters to the crystallite size is reported by Melcher [43] and Bergmann [44].

The as-synthesized YET particles were characterized by Photon

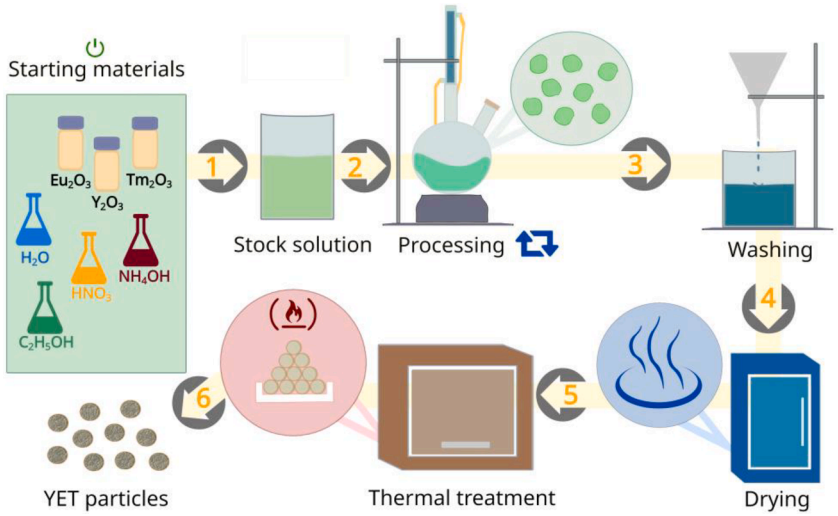

Fig. 1. Hydrothermal synthesis performed in the study to produce europium thulium co-doped yttria powders (YET).

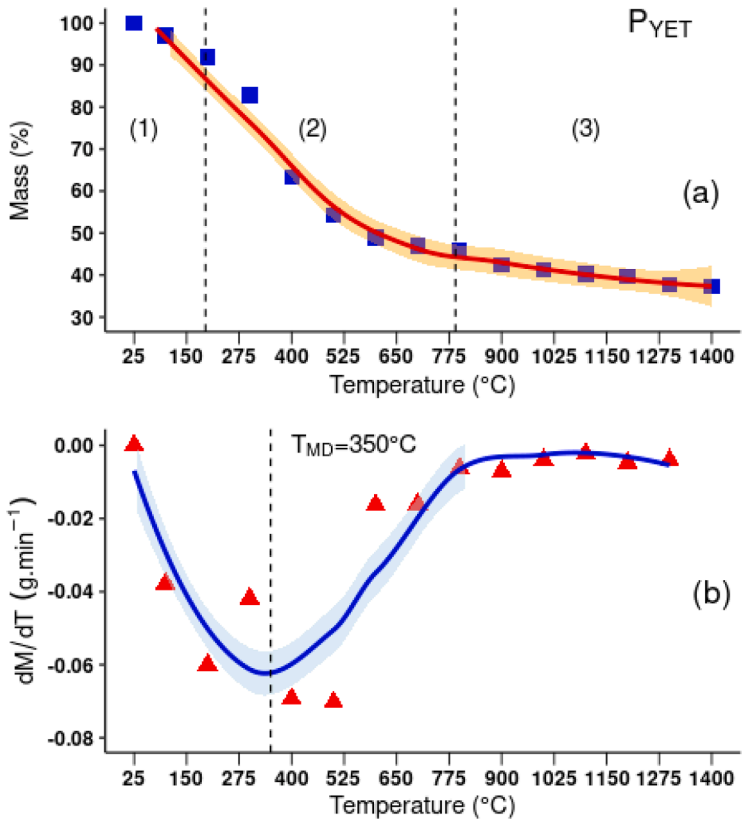

Fig. 2. Thermal decomposition of the powdered precursor (P_{YET}) up to 1400ºC in air atmosphere during a heating rate of 5ºC.min^{-1}.

Correlation Spectroscopy (PCS, Litesizer500, Anton Paar) in order to determine the particle size distribution (d_{10},d_{50}, and d_{90}), where the hydrodynamic diameter of particles (d_h) was calculated based on the hydrodynamic diameter model as shown in (Eq.2) [45]. Besides, to carry out the characterization the following parameters such as diluted aqueous suspensions (0.05%vol particles), equilibration time 10s, number of runs 5, evaluation time 20s, and temperature 25°C were used.

$$d_h = \left(\frac{K_{BT}}{3\pi\eta(T)D_t}\right)[nm] \quad (2)$$

Where, K_{BT} is the Boltzmann constant (1.38064852.10^{-23}m^2.kg.s^{-2}. K^{-1}), T is temperature (K), (T) is viscosity of the suspending liquid and, D_t is particle diffusion coefficient.

Solid density (ρ_s) of the YET powders was evaluated by using a helium gas pycnometer (Micrometrics 1330), where ρ_s-value is achieved according to Eq. 3 [46].

$$\rho_s = \left(\frac{w}{V_p}\right)[g.cm^{-3}] \quad (3)$$

Where, w is the weight of sample, and V_p is the powder volume.

The specific surface area (S_{SA}) of the YET powders were determined by gas adsorption method, using a surface analyser (ASAP2010, Micrometrics). This method proposed by Bruaner, Emmett, and Teller [47] is known as BET. The S_{SA} of powders by unit of mass is expressed in Eq. 4 [47].

$$S_{SA} = \frac{N_A V_M A_M}{V_{mol} M_s}[m^2.g^{-1}] \quad (4)$$

Where N_A is the Avogadro constant (6.023×10^{23}); V_M is the volume (cm^3) of the adsorbed gas molecule; A_M is the area in which the adsorved gas molecule covers (16.2×10^{-20}m^2 for N_2); V_{mol} is 1mol volume (cm^3) of the gas at environmental temperature; and M_S is the mass (g) of sample.

The quantification of specific surface area (S_{SA}) can involve direct measurement of particle size (d_{BET}), as expressed in Eq.5. In this relation is considered that the shape of particles is spherical and uniform.

$$d_{BET} = \frac{6}{\rho_t . S_{SA}}[\mu m] \quad (5)$$

Where ρ_t is the theoretical density of sample; S_{SA} is the specific surface area of sample

The state of agglomeration of particles reveals how much particles that constitute the powdered sample are agglomerated, and is the ratio of the mean particle diameter (d_{50}) measured by laser diffraction and particle size obtained directly by BET method (d_{BET}), as shown in Eq.6. As Fag is 1 indicates particles are uniform and dispersed, while Fag is less than 1 suggests differences of shape form (length/ radius) among particles. However, as Fag is more than 1 particles are agglomerated.

$$F_{ag} = \frac{d_{50}}{d_{BET}} \quad (6)$$

The shape and size of the YET powders were observed by Scanning Electron Microscopy (SEM, INCAx-act, Oxford Instruments).

Paramagnetic response of YET powdered compositions as-synthesized and irradiated with 5kGy (γ-radiation, ^{60}Co) were evaluated by electron paramagnetic resonance using a X-band EPR spectrometer (Bruker EMX PLUS), under room temperature and atmosphere. The EPR spectra of samples were recorded in field modulation frequency of 100kHz, microwave power of 2.5mW, center field of 300mT, sweep width of 300mT, modulation amplitude of 0.4mT, time constant of 0.01ms, 10 scans, temperature of 20ºC, environmental atmosphere, under controlled humidity, and using DPPH (2, 2-Diphenyl-1-picrylhydrazyl, Bruker) as EPR reference.

$$\Delta E = h\nu = g\mu_B\beta_0 \quad (7)$$

Where h is the Planck's constant (6.626 10^{-34}J.s), μB is the Bohr

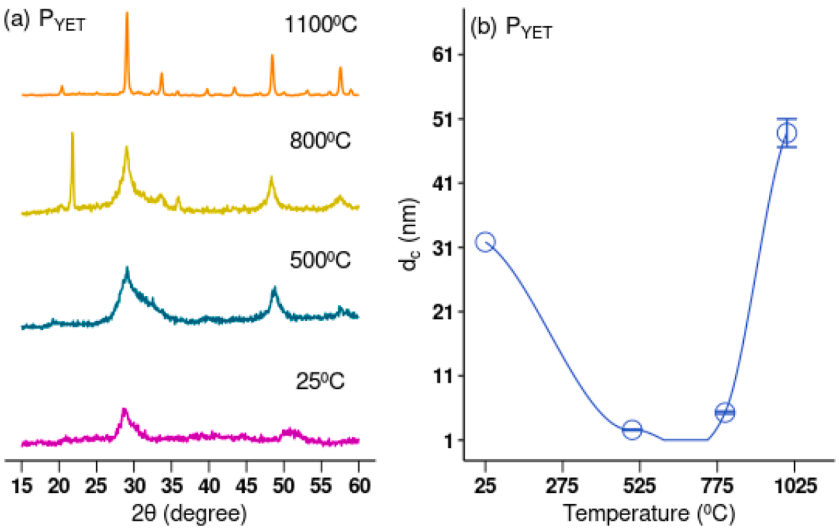

Fig. 3. Formation and structural evolution of europium-thulium-yttria powders obtained by hydrothermal method: (a) XRD curves of the precursor powders (P_{YET}) annealed up to 1100ºC; and (b) variation of the crystallite size (d_c) of samples as a function of annealing temperature.

magneton (9.274×10^{-24}J.T^{-1}), g is the gyromagnetic ratio, B_0 is the magnetic field in gauss (G), and v is the microwave frequency in hertz (GHz).

$$g = 714.4775\left(\frac{v}{B_0}\right) \quad (8)$$

3. Results and discussion

Hydrothermal synthesis provides the formation of nano-structured materials with homogenous phase and controlled particle size distribution, where a powdered precursor substance is subjected of annealing in order to become a crystalline material. The thermal decomposition of the powdered precursor (P_{YET}) as a function of annealing temperature illustrated in Fig. 2a reveals three distinct regions of decomposition. The region (1) ranging from environmental temperature (~25ºC) to 165ºC

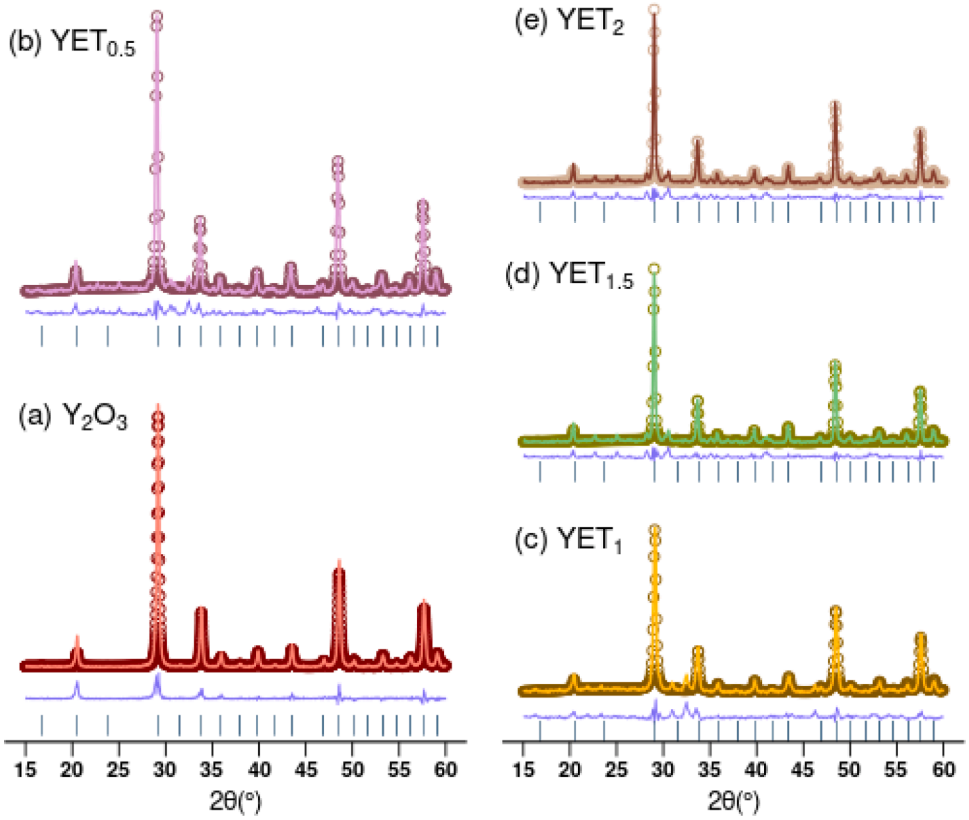

Fig. 4. Rietveld refinement of the powder pattern of YET compositions (YET_x, x ranging from 0.5-2at.%Tm, and Y_2O_3 is "pure" yttria). Solid line is the experimental data, circles are the calculated pattern, slateblue line is the difference pattern (experimental - calculated), and skyblue points are the indexed peaks according to BGMN structure file 04-005-4378.

which corresponds to 12% mass, was due to the broken down of weak bonded water molecules (hydration); region (2) ranging from 165ºC to 778ºC as a result of decomposition of yttrium nitrate -$Y(NO_3)_3$ and represents the greatest sample decomposition, corresponding to 41% mass loss; and (3) ranging from 778ºC until the end of the assay (1400ºC), corresponding to 5% mass loss. The accumulated mass loss observed during the assay up to 1400ºC was 59%.

Additionally, the first derivative of the mass loss curve (Fig. 2a) shown in Fig. 2b reveals that the temperature where the maximum mass loss was observed at 350ºC and fits suitably with the previous result observed in Fig. 2a, considering that the great decomposition of the powdered precursor occurs in the range of temperature from 165ºC to 778ºC. Moreover, above 900ºC up to 1400ºC a slight mass loss was observed, which suggests that the formation of of thulium-europium-yttria particles in crystalline form takes place in this range of temperature.

With the aim to prove the hypothesis presented previously, three annealing temperatures as 500, 800, and 1100ºC were proposed as thermal treatment of the powdered precursor (P_{YET}) and the crystalline evolution of samples was followed by XRD as illustrated in Fig. 3a. The as-synthesized sample (pink solid line) presented an amorphous spectra, having as characteristic a short range peak recorded at 29.5°(2Θ). The beginning of structural transition from amorphous to crystalline form is observed from temperature of 500°C (green solid line), exhibiting two short range peaks recorded at 29.5° and 50, whereas at 800°C (yellow solid line) a sharp peak was recorded at 21.5°. Finally, the powdered precursor treated at 1100°C (orange solid line) exhibited a crystalline spectra, corresponding to C-type structure, with the main diffraction peaks recorded at 29.5°, 53.0°, and 57.6°.

Additionally, the changes on crystallite size (d_c) of the P_{YET} as a function of the temperature of thermal annealing illustrated in Fig. 3b revealed that the as-synthesized powders presented a d_c of 31nm ascribed to yttrium-nitrate based aggregates formed from hydrothermal synthesis. By rising the annealing temperature to 500 and 800ºC, the d_c of P_{YET} reduced remarkably to 2 and 6nm respectively due to decomposition and structural transition of P_{YET}. Moreover, annealing at 1100ºC provided an increase of d_c to 52nm due to the formation of crystalline form (from amorphous to cubic C-type), including aggregation of particles as a result of mass transport at high temperature. To control the increase of crystallite size and aggregation of particles researchers have proposed innovative synthesis methods. Tlili et al. [48] by a combination of the sol–gel and mechanical milling with milling time up to 2h observed that the reduction of the crystallite size from 26 to 9nm of $La_{0.6}Sr_{0.35}Ca_{0.05}CoO_3$ samples provided the decrease of the Curie temperature, magnetization values, and broadened the phase-transition region of these materials. Zhang et al. [49] successfully prepared Si crystallites (10nm) by a controlled thermal reduction method based on Mg_2Si alloy powder as a reducing agent, amorphous SiO_2 as a precursor, and ball-milling process.

Rietveld refinement performed for all powder pattern of YET compositions, including "pure yttria" (Y_2O_3) are illustrated in Fig. 4. Yttria as a host material (Fig. 4a) exhibited cubic C-type form, with high intense diffraction peak recorded at 29.5°, space group C_2 and C_{3i},S_6, with an R-factor (R_{wp}) 20.77%, and crystal density (ρ_{XRD}) of 5.031g.cm^{-3}. Rietveld refinement of the $YET_{0.5}$ pattern obtained by annealing of the P_{YET} at 1100ºC illustrated in Fig. 4b confirms that the ceramic powders exhibited a cubic C-type structure (orange solid line), composed by sixteen unit formula, C_{3i}, S_6 space group, with a precision fitting (red circle points) in which (Rw) was 17.59, and crystal density (ρ_{XRD}) of 5.03.gcm^{-3}. As reported by Couteres et al. [50] the cubic C-type form is the predominant structure for most rare earth sesquioxides (RE_2O_3), even though the type of crystal structure of yttria can be A-type (monoclinc), B-type (hexagonal), and C-type (cubic). Some studies [51–53]reported that the forms A\B-type of yttria are achieved under high temperature and pressure. On the other hand, C-type form is the most common structure of yttria, being stable even in high range of temperature (800°C < T < 2400°C). Furthermore, the present results reveal that cubic C-type yttria based nanoparticles can be formed under thermal treatment at 1100°C for 2h, and the use of europium and thulium as activators did not change the crystalline form of yttria (C-type form, BGMN structure file 04-005-4378), which evidences a substitutional character of co-doping. It is not evidenced any substantial difference in crystalline structure of other compositions of YET (Fig. 4c – 4e), the refining results revealed a very small noise from the obtained patterns and calculated ones (purple curves), and the following Rw and ρ_{XRD} values for all samples evaluated are shown in Table 2.

Table 2
Results of Rietveld refinement of the YET powdered compositions.

Composition	ρ_{XRD} (g.cm^{-3})	R_{wp} (%)	Lattice parameter [a] (nm)	Structure
Y_2O_3	5.03	20.77	1.060420±0.000042	Cubic C-type
$YET_{0.5}$	5.03	17.59	1.060595±0.000076	
YET_1	5.03	18.14	1.060595±0.000010	
$YET_{1.5}$	5.03	18.15	1.060676±0.000079	
YET_2	5.03	13.87	1.060595±0.000076	

Composition: YET_X, x ranging from 0.5-2at.%Tm, and Y_2O_3 is "pure" yttria; ρ_{XRD} is the sample density calculated by Rietveld refinement; R_{wp} is the goodness refinement index.

Therefore, the results revealed that the co-doping process of yttria with europium (2at.%) and thulium (0.5-2.0at%) did not promote remarkable changes in crystalline structure of yttria, where all samples exhibited cubic C-type form. This result is in accordance with our recent study on europium-yttria nanoparticles [38], and with the solidification diagram of the rare earth sesquioxides (RE_2O_3) [50], where the cubic C-type form is the most predominant crystalline phase for Y, Eu, and Tm based sesquioxides. In addition, the crystallite size (d_c) of the YET powdered compositions increased according to Tm content (Fig. 5). However, from 0.5 to 1.0at.%Tm the slight decrease of d_c may be attributed to the relaxation of strain that occurred in the lattice. Apart from 1.0 up to 2at.%Tm a substantial increase of d_c was noticed, and may be attributed to the replacement of Y ions by Tm ions in the crystal lattice, resulting in expansion of the unit cell volume. Nevertheless, as nanoparticles have secondary phases the increase of d_c is not directly proportional to dopant content, as reported by some authors [54–56].

The material properties usually rely on the type of chemical bonding between the elements that form its structure, on the microstructure, and on the electronic distribution structure. From a solid state perspective, the distribution of the electrons, including their orientation have a great effect on the material response such as luminescence [57], mechanical strength [58], magnetism [59], and thermal conductivity [60]. The electron density distribution is related to the coordination of the elements (atoms/molecules), which form the chemical environment in a crystal lattice, and can contribute to elucidate a particular property of a material. In terms of radiation dosimetry, the capacity of a material to provide a suitable dose-response behaviour is a requirement.

The electron density maps of the YET compositions obtained in range of -1.46 to +1.46e$Å^{-3}$, AB projection, electron map voxel size of 0.40Å, and $F_{obs} - F_{calc}$, are illustrated in Fig. 6a. At low density region, it is noticed that "pure" yttria exhibited mostly medium and low sites of electron density (yellow, green, and blue contours) due to yttrium (Y) atoms are majority surrounded by few oxygen (O) atoms and vacancies, while at high density region few sites of high density were formed due to the presence of Y atoms surrounded by three O atoms (red contours). Doping yttria with europium (Eu) and thulium (Tm) induced changes on its electron density distribution. At low density region, it was observed that the electron density around element sites ($YET_{0.5}$ and $YET_{1.5}$ compositions) was very low compared to high dose region (few red contour lines). Besides, $YET_{0.5}$ composition presented the highest electron density among all compositions prepared. From atomic view (electrons, protons and neutrons), it is stated that all protons are situated in the nucleus, and the presence of the nucleus can be observed in sites with

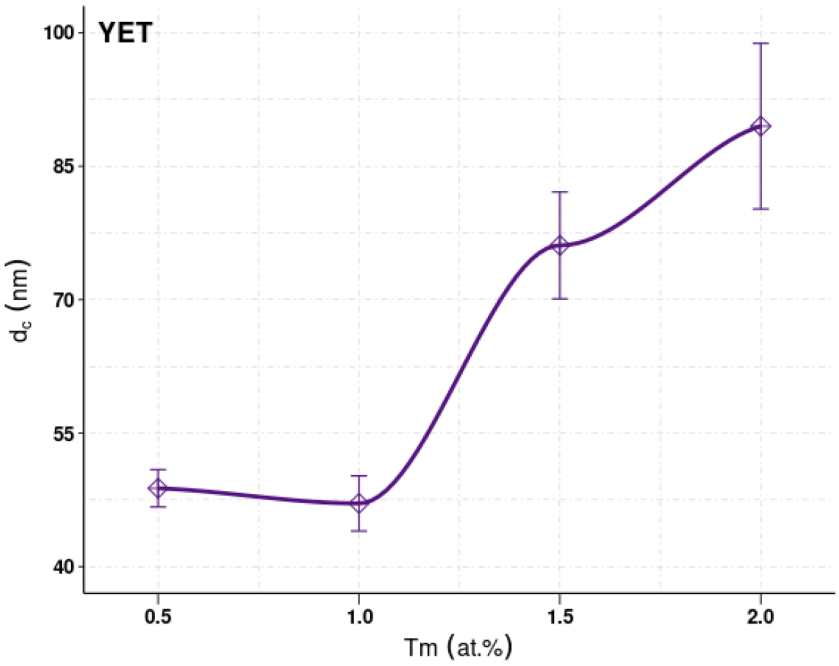

Fig. 5. Variation of the cristallite size (d_c) of the YET powders as a function of thulium content (atomic percentage, at%Tm).

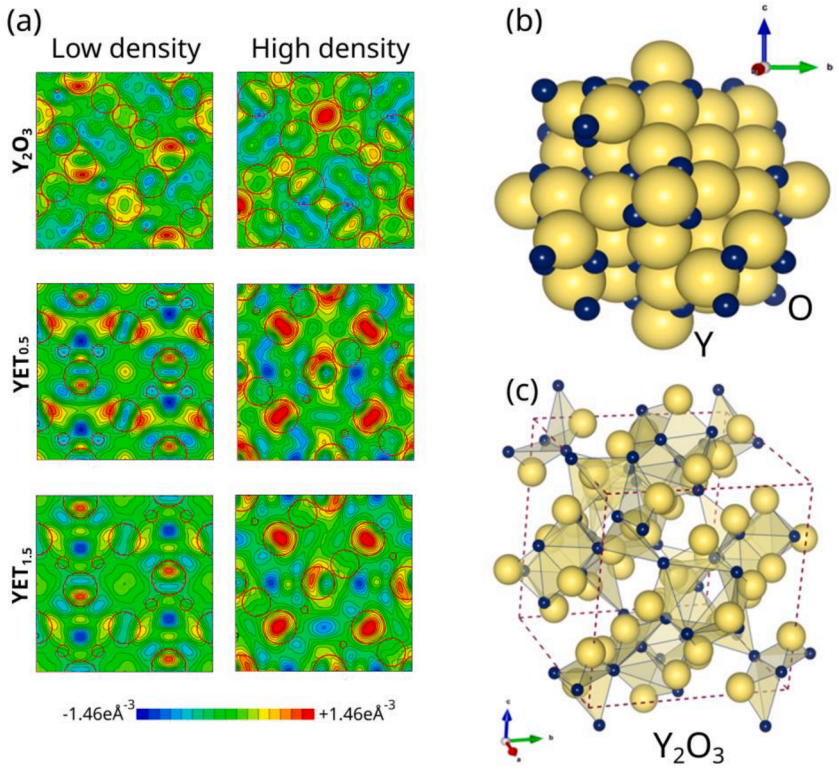

Fig. 6. Crystal features of the YET powdered compositions prepared with up to 1.5at.%Tm: (a) electron density maps; and representations of the unit cell of yttria as (b) ball-and-stick model; and (c) polyhedral ball-thick model.

positive charge density values. The insertion of europium and thulium into yttria lattice, where Tm and Eu have atomic numbers (Z) of 69, and 63 respectively, and larger than Y (39), lead to imply that theirs nucleus contain the highest number of protons. Moreover, it is seen that the similarity of the electronegative character of the rare-earth constituents (Y, Eu, Tm) led to deformation of the high density sites (red contour lines), which indicates an electron path through rare-earth constituents. Therefore, the results indicate that $YET_{0.5}$ clusters have high-charge density regions improved by the presence of Tm and Eu activators.

The unit cell of yttria is represented by topological models [61] as ball-and-stick (Fig. 6b) and polyhedral-ball-thick (Fig. 6c), respectively. The unit cell contains 16 formula units, with 32 cations that constitutes 24 sites of C_2 symmetry, including 8 sites of C_{3i} symmetry. Besides, the Y atoms (gold) are octahedrally coordinated by O atoms (dark blue) as

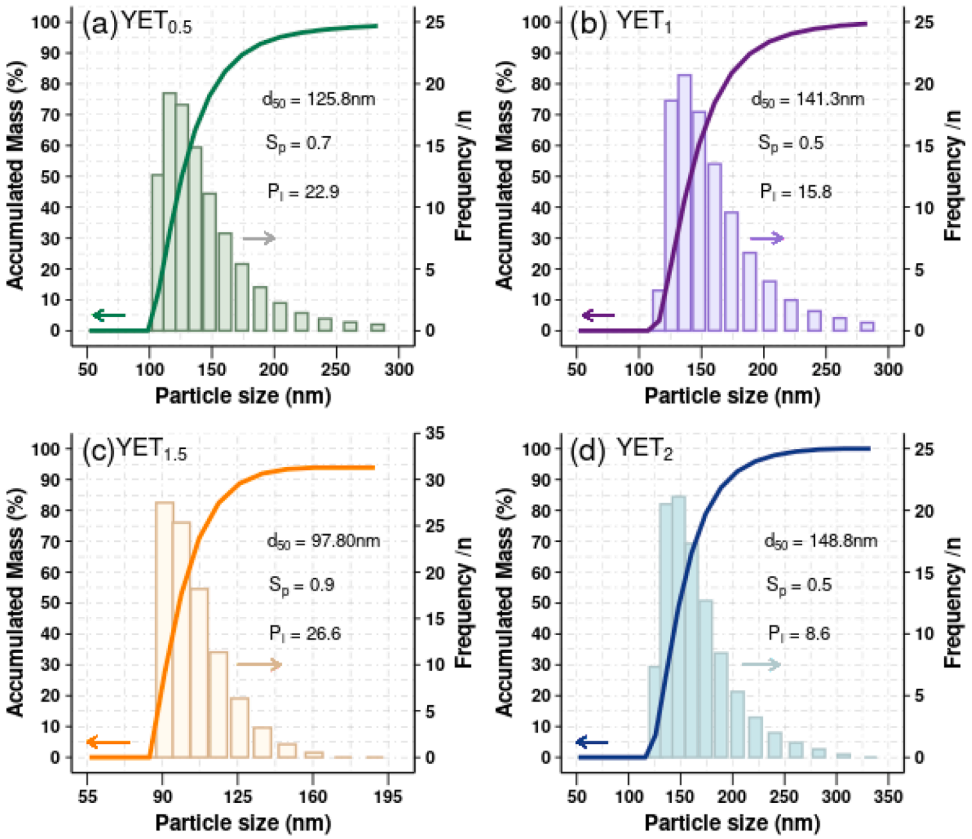

Fig. 7. Particle size distribution of YET powdered compositions by PCS: (a)$YET_{0.5}$, (b)YET_1, (c)$YET_{1.5}$, and (d)YET_2. d_{50} is the mean particle size corresponding to 50% fraction (accumulated mass); Sp is span - the particle size difference between d_{90} and d_{10} fractions; P_I is the polidispersity index.

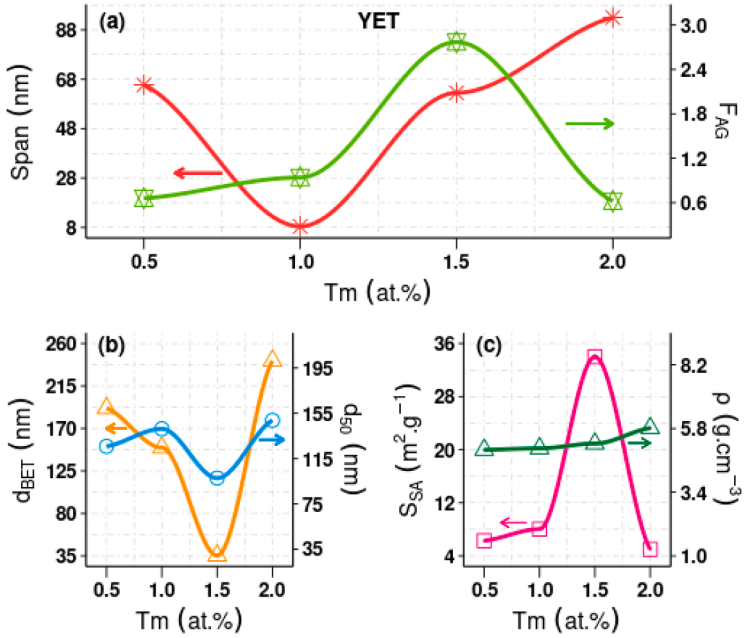

Fig. 8. Particle characteristics of YET powdered compositions: (a) Span x F_{AG}, (b) d_{BET} x d_{50}, and (c) S_{SA} x ρ. Sp is span, the particle size difference between d_{90} and d_{10} fractions; F_{AG} is the agglomeration factor; d_{BET} is the particle size calculated from specific surface area (S_{SA}) data; d_{50} is the mean particle size; and ρ is the pycnometric density.

illustrated in Fig. 6b. As evidencied by Rietveld refinement results (Fig. 4), the dopants used (Tm^{3+} and Eu^{3+}) uniformly replaced Y^{3+} ions in sites (C_2; S_6,C_{3i}), which means no formation of second phases neiher disordered of the lattice.

Particle size distributions of YET powders illustrated in Fig. 7 revealed that all samples exhibited a narrow particle size distribution, where a mean particle size (d_{50}) was less than 150nm. In addition, the YET 1.5 powders presented the smallest d_{50} of 97nm among all

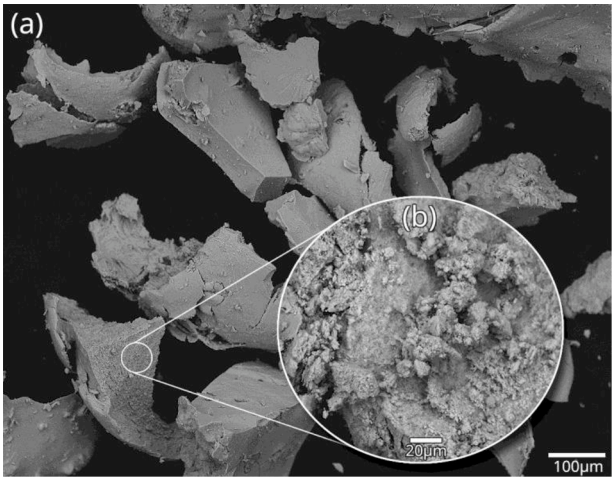

Fig. 9. SEM images of YET powders containing 0.5at.%Tm: (a) general view of agglomerate of particles with plate shape and size higher than 100μm, and (b) internal view of a powdered agglomerate, revealing thinner particles whose size is in nano scale range.

compositions obtained. However the highest poly-dispersion index (PI) of 26.6 was recorded for this composition, due to the effect of attraction forces on thinner particles that produces large agglomerate of particles. Additionally, the difference between the fraction distributions d_{90} and d_{10} (span, S_p) varied from 8 to 89nm (Fig. 8a), which corresponds to 91.75% of $YET_{1.5}$ d_{50}. Moreover, the agglomeration factor (F_{AG}) which is the ratio of d_{50} and d_{BET} increased as Tm content increased, except for YET_2 composition, and indicates that YET particles tend to agglomerate easily due to their nano scale. The values of d_{BET} (Fig. 8b) varied from 35-242nm according to YET composition (0-2at.%Tm). It is important to emphasize the difference between d_{BET} and d_{50} values, where the first is calculated based on SSA results, considering gas adsorption phenomena over all particulate system, while the second come from laser diffraction due to Brownian motion of particles. Furthermore, d_{BET} can be considered a precision parameter that expresses as near as possible the real size of the particles. The pycnometric density (ρ) of YET compositions did not alter considerably as Tm content increased due to low concentration of the dopant.

The results illustrated in Fig. 8a-8c reveal that co-doping yttria with Tm by hydrothermal synthesis provided changes on particle characteristics such as, particle size distribution (d_{10}, d_{50}, d_{90}), agglomeration factor (F_{ag}) specific surface area (S_{SA}), and pycnometric density(ρ). The particle size is a key issue in powder processing, seeing that it affects further stages of processing such as mixing, dispersion, shaping, and sintering. Besides, it changes the characteristics of the powdered material, including the final characteristics of the material. Liu et al. [62] observed that the ultraviolet light scattering coefficient of gray Si_3N_4 based particles decreases as the particle size increases. Pu et al. [63] improved considerably the microstructure and mechanical properties of TiP/VW94 composites, by using Ti particles as reinforcement (d_{50} 1-7μm and 10-55μm), where elongation increased by 48%. Chen et al. [64] observed that the viscosity of the alumina suspensions decreases as the fraction of fine powder increases. In addition, samples prepared with 0.1 fraction of fine powder and sintered at 1550°C exhibit a flexural strength of 78.15 ± 3.50 MPa and porosity of 30.12 ± 0.08%.

SEM images of YET powders with 0.5at%Tm illustrated in Fig. 9 reveal that the proposed synthesis method provided plated-like powdered agglomerates of size higher than 100μm (Fig. 9a). These large agglomerates are constituted by thinner particles (Fig. 9b) that are bonded together weakly due to the action of attraction forces, forming a particulate net. Taking in account that the size of these particles are in nano scale range and the SEM equipment has a limited resolution to

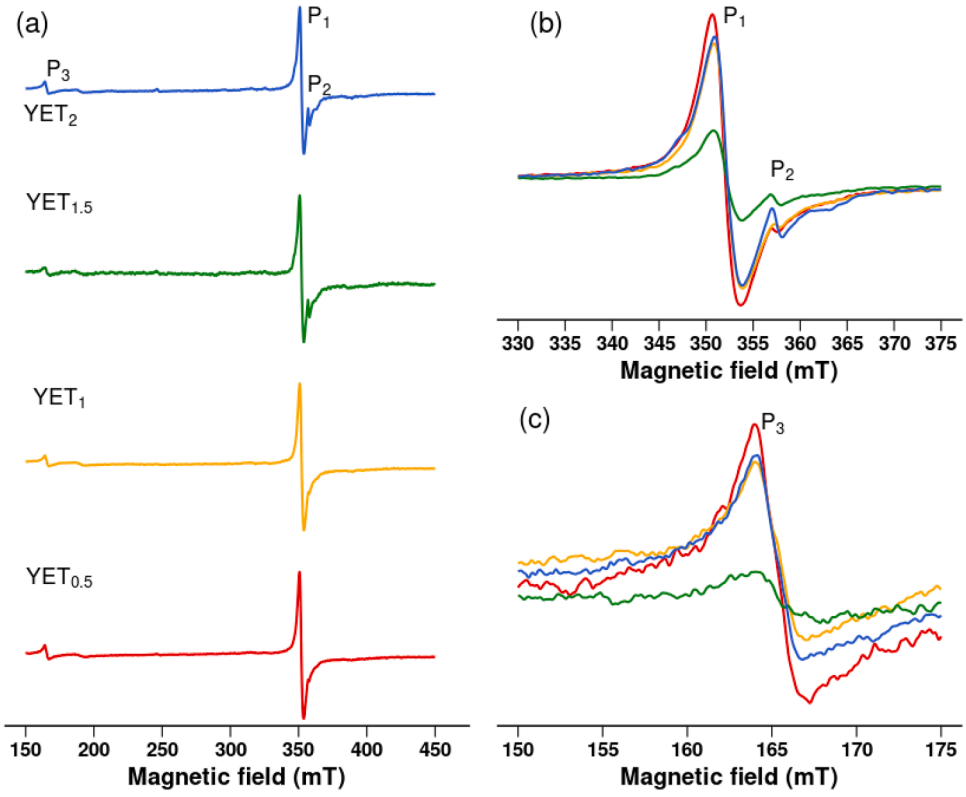

Fig. 10. EPR spectra of YET powders prepared with up to 2at.%Tm by hydrothermal synthesis, followed by annealing at 1100°C for 2h in air atmosphere, and recorded in a range of magnetic field (a) from 150 to 450mT (general view); (b) from 330 to 375mT and highlighting P_1 and P_2 peaks; and (c) from 150 to 175mT, showing P_3 peak.

Table 3
EPR parameters of the YET powdered compositions as-synthesized.

YET (at.%)	g-value			Peak width (mT)		
	P_1	P_2	P_3	P_1	P_2	P_3
0	1.99089	1.96574	-	6.56	1.08	-
0.5	1.98887	1.98124	4.29021	3.00	4.92	3.28
1.0	1.98774	1.98124	4.29916	3.04	4.92	3.08
1.5	1.98744	1.98124	4.28811	3.04	1.80	3.80
2.0	1.98796	1.98124	4.28602	2.88	1.96	2.68

YET (0at.%) refers to Y_2O_3; "-" not available; P_1, P_2, and P_3 are the EPR peaks observed in YET compositions.

observe thin powders, unfortunately, the SEM image illustrated in Fig. 9b did not reveal clearly the shape of YET particles. However, in our previous study [38], rounded thulium-yttria particles were obtained by performing this same synthesis method. Like particle size, the shape of particles can have influence on ceramic processing, as well as, on the final features of the material/component produced. Innovative approaches have been reported to control the shape of particles, providing particles with smart shapes such as, flow-like [65], solid cube [66], hollow cube [66], from nanorods to nano-spherical [67], and flow-like to mesoporous [68].

Co-doping yttria with europium and thulium (YET) has the aim to improve the EPR response of yttria by promoting new electron defects (traps and radicals). These traps can improve the capacity of the host material (yttria) to keep the energy received from ionizing radiation (dose) and release it under a procedure of stimulation. The energy released by the material as stimulated is usually proportional to the dose, a condition that indicate the ability of a material to "measure" the dose applied during a procedure in which ionizing radiation was used and it is the aim of dosimetry.

The EPR spectra of YET compositions prepared with up to 2at% Tm are illustrated in Fig. 10. The results indicate that YET samples exhibited three EPR peaks assigned as P_1, P_2, and P_3 which position recorded in the magnetic field, g-values, and peak widths changed due to Tm content (Table 3). The position of P_1 peak was recorded in a range of magnetic field from 348.64 to 349.82mT, while P_2 and P_3 peaks were recorded in a range of magnetic field from 348.64 to 349.82mT, and from 163.72 to 163.92mT, respectively. The main peak P_1, with and g-value ranging from 1.98744 to 1.99089, is due to adsorption of the oxygen from the thermal annealing atmosphere [69], forming interstitial O^{2-} ion as observed previously by Osada et al. [70] for Y_2O_3-CaO based samples, Singh et al. [71] for Er:Y_2O_3 powders, and Bordun et al. [72] for "pure" yttria. Additionally, the peak P_2 recorded in a range of magnetic field from 356 357mT, line width varying from 1.40 to 4.68, and g-value ranging from 1.96574 to 1.98124 is ascribed to F^+ centers, i.e oxygen vacancies containing a remaining electron. Moreover, the peak P_3 recorded in a range of magnetic field from 163.72 to 167.84mT, line width varying from 2.68 to 3.80mT, and g-value ranging from 4.28811 to 4.29021 can be ascribed to the presence of Tm^{3+} ions integrating yttria lattice. Such result was also noticed during our last investigation on Tm:Y_2O_3 rods produced by bio-prototyping, where peak P_3 was recorded at 367.64 mT, with a line width of 1.0mT, and g-value of 1.9162.

Considering the recent achievements on EPR characterization of yttria based materials reported by our group, including the new findings presented in this study, it is noticed that the conditions of synthesis and processing of particles have a great influence on the EPR response of yttria. During our recent study on "pure" yttria rods [32], two EPR peaks (p_1 and p_2) were observed, where p_1 was recorded at 352mT, with a g-value of 2.020, and a line width around 2.3mT, whereas p_2 was recorded at 357mT, with a g-value of 2.040, and a line width around 2.3mT. Moreover, it was noticed that the incorporation of RE ions in yttria structure leads to significant changes on its paramagnetic features. Europium-yttria micro rods exhibited four EPR peaks assigned as (a) and (b) recorded at 163.5 mT and 248.0 mT, with g-values of 4.2960 and 2.8540, respectively. The main peak c_1 was recorded at 352mT, with line width of 6mT and g-value of 2.0040, whereas c_2 was recorded at

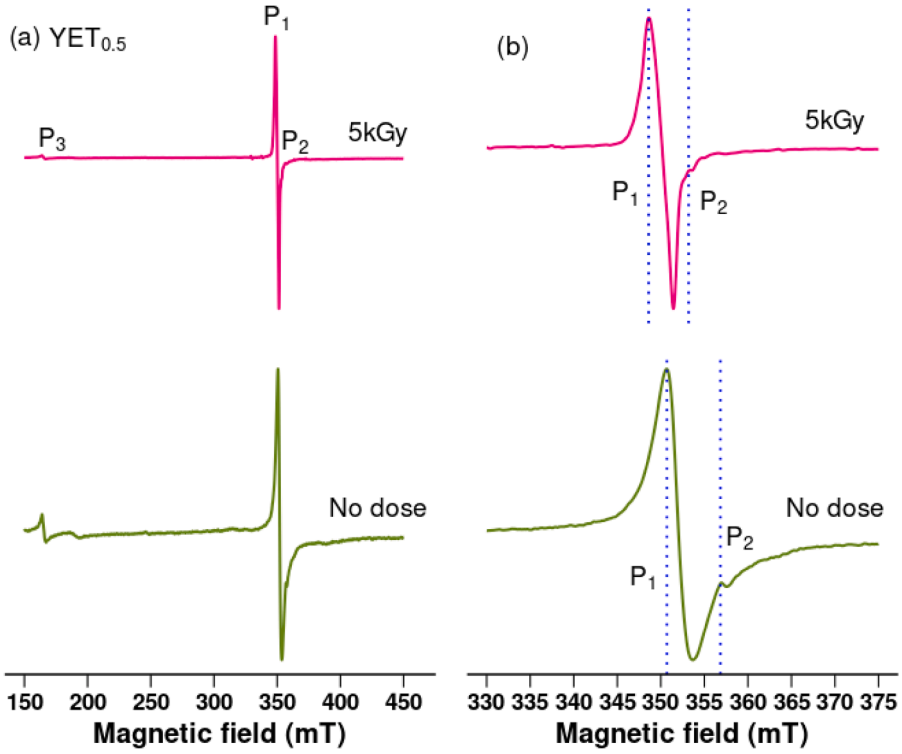

Fig. 11. EPR spectra of $YET_{0.5}$ powdered composition as-synthesized (no dose – green line) and irradiated with 5kGy (magenta line), recorded in a range of magnetic field (a) from 150 to 450mT with the following resonance peaks P_1, P_2, and P_3; (b) from 330 to 375mT, where the radiation effect on peak shape, peak width, and peaks positions (P_1 and P_2) of samples was evidenced.

Table 4
EPR parameters of the YET powdered compositions irradiated with 5kGy.

YET (at.%)	g-value			Peak width (mT)		
	P_1	P_2	P_3	P_1	P_2	P_3
0	2.01036	1.97037	-	2.00	1.96	-
0.5	2.01799	1.98125	4.29337	2.80	4.74	2.72
1.0	2.01738	1.97991	4.29468	3.20	4.68	3.68
1.5	2.01663	1.97791	4.29884	2.84	1.40	4.00
2.0	2.01798	1.98051	4.29449	2.76	1.64	2.76

YET (0at.%) refers to Y_2O_3; "-" not available; P_1, P_2, and P_3 are the EPR peaks observed in YET compositions.

357mT, with line width of 1.8mT and g-value of 1.9690. While thulium-yttria powders (Tm:Y_2O_3) exhibited an EPR spectra with two resonance peaks (P_1 and P_2) recorded at 350 mT and 164 mT, respectively. [38] On the other hand, the peak P_2 was not observed in the EPR spectra of Tm:Y_2O_3 rods sintered at 1600°C for 2h in air atmosphere, which reveals that peak P_2 is not stable at high temperature. [39]

The EPR spectra of $YET_{0.5}$ powders as-synthesized and irradiated with 5kGy are illustrated in Fig. 11. The results presented in Fig. 11a reveal that irradiated samples exhibited sharpen EPR spectra, in which the main peak P_1 peak recorded with a range of g-values from 2.01036 to 2.01799 showed a narrow shape, while the peaks P_2 and P_3 recorded with a range of g-values from 2.01036 to 2.01799 (Table 4), and recorded with a range of g-values from 2.01036 to 2.01799, respectively. Besides, this peaks presented lower intensity as compared to the spectra of the as-synthesized powders. This result evidences the instability of P_2 and P_3 peaks under high dose irradiation. Moreover, as illustrated in Fig. 11b, the irradiation with 5kGy promoted a little shift of the resonance peaks (P_1, P_2), from 350.7mT to 348.6mT and 350.7mT to

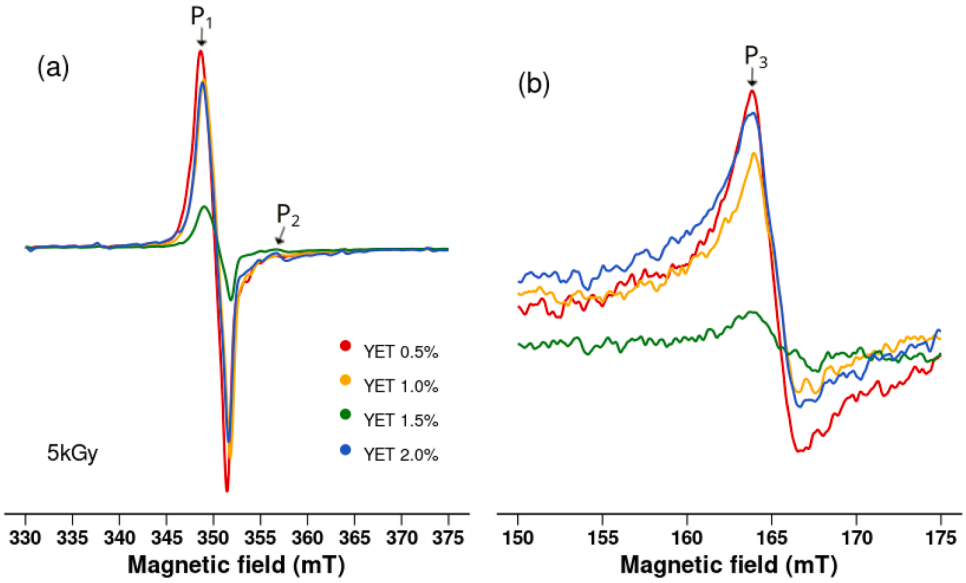

Fig. 12. EPR spectra of YET powdered compositions with up to 2at.%Tm as irradiated with 5kGy dose (^{60}Co), and recorded in a range of magnetic field (a) from 330 to 375mT, with the resonance peaks P_1 and P_2; and (b) from 150 to 175mT, with the resonance peak P_3.

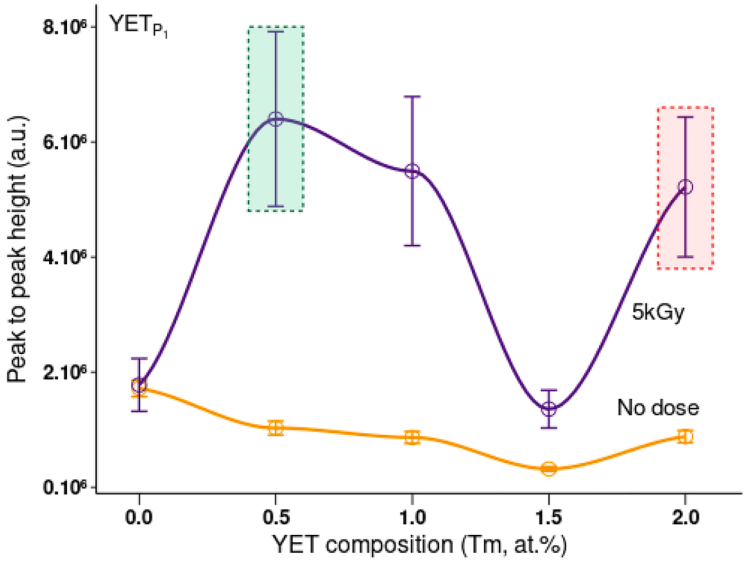

Fig. 13. Peak to peak height of the EPR response of the YET powdered compositions prepared with up to 2at.%Tm. The orange curve represents samples with no dose (as-synthesized), whereas the purple curve represents the irradiated ones with 5kGy (^{60}Co). The green rectangle indicates the composition with most intense peak to peak EPR response, while the red rectangle suggests the one with behaviour of recombination trough defects, leading to decrease of the peak to peak EPR signal.

353.2mT, respectively.

The irradiation effect on promotion of EPR spectra of YET powdered compositions is illustrated in Fig. 12. According to results, non-additional resonance peak was observed in any compositions. The $YET_{0.5}$ sample presented the most intense EPR signal among all compositions prepared. The main peak P_1 exhibited a sharp and narrow shape, while it was noticed that the intensity of peak P_2 was reduced considerably, which indicates that the radical is not stable under high dose irradiation. On the other hand, the peak P_3 remained stable and with higher intensity. The present results reveal that YET samples with distinct compositions presented a sensitivity to ionizing radiation, in which the $YET_{0.5}$ composition exhibited the most significant result.

As result of co-doping, the activators selected in this study (Eu, Tm) improved considerably the EPR response of yttria as shown in Fig. 13. The peak to peak height of the main peak P_1 was considered as a reference. It is clearly evidenced that no irradiated samples presented low EPR response, being less than 2.10^6a.u., due to the low number of radicals formed during synthesis and processing. However, this scenario changed remarkably as samples were irradiated with 5kGy, where the peak to peak EPR signal achieved values three times higher than those of no irradiated samples. Besides, the $YET_{0.5}$ sample exhibited the highest peak to peak EPR response among all compositions prepared (highlighted by a green rectangle), in accordance with those results reported previously and illustrated in Fig. 11a and 11b.

Moreover, the $YET_{1.5}$ composition (Fig. 13) presented the lowest EPR response of all, while the $YET_{2.0}$ composition exhibited a great EPR response (highlighted by red rectangle) due to recombination of electron defects. It has been noticed in EPR studies on yttria based materials reported by the group that the addition of great quantity of rare-earth dopant does not improve the EPR response of yttria, in fact it has an undesired effect on it, by reducing the EPR response to ionizing radiation. Europium-yttria rods prepared with 10at.%Eu exhibited low EPR peak to peak response in a range of dose from 0.001 up to 100kGy, whereas those containing 2at.%Eu presented higher peak to peak EPR response, and with linear behaviour in a range of dose from 0.001 to 10 kGy. [33] During the study on thulium-yttria particles doped with up to 2at.%Tm (thulium) [38], it was noticed that as-synthesized powders with 2at.%Tm exhibited the highest peak to peak EPR response. On the other hand, powdered compositions with 0.1 and 0.3at.%Tm presented outstanding peak to peak EPR response among all compositions.

Yttria has as intrinsic features great number of oxygen vacancies and symmetry axis C_2, and C_{3i}, S_6. As a great quantity of dopant is used e.g. rare-earth dopant (RE), most of it can be located at C_{3i},S_6 axis, where the probability of electron transitions is low i.e the EPR response is also low. Besides, increasing the quantity of dopants in a host material reduces directly the distance between RE-ions in its lattice, which in turn leads to more interference between them, and concentration quenching. On the other hand, when RE-ion is located at C_2 symmetry, the electron transitions are facilitated, resulting in higher EPR response. Therefore, using lower quantity of rare-earth dopants usually provide substantial number of electron defects in yttria lattice and enhance its capacity to trap a higher number of unpaired electrons as it is subjected to ionizing radiation. The present achievements reveal that $YET_{0.5}$ composition exhibits the most effective EPR dose-response signal and indicate that this material is worth of studying to develop advanced materials for radiation dosimetry.

4. Conclusion

Europium-thulium-yttria (YET) powdered compositions containing up to 2at.%Tm, with cubic C-type form, mean particle size less than 150nm, and electron paramagnetic resonance (EPR) response, were produced by a relative low temperature hydrothermal synthesis, followed by annealing at 1100°C for 2h in air atmosphere. YET nanoparticles prepared with 0.5at.%Tm exhibited the most significant peak to peak EPR response as irradiated with 5kGy among all compositions. The present results demonstrated that YET nanoparticles are promising materials for new dosimetric components.

Funding

The authors would like to acknowledge the following sponsor organizations: São Paulo Research Foundation (FAPESP, grant# 2018/05982-0; grant# 2022/06695-0), National Council for Scientific and Technological Development (CNPq, grant# 426513/2018-5), and Coordination for the Improvement of High Degree People (CAPES, grant# 88882.315568/2019-01).

Ethics and Consent to Participate

No human or animal were used in the study.

Consent for Publication

We authors declare our consent for publication.

Data availability

- The raw/processed data required to reproduce these findings cannot be shared at this time due to technical or time limitations.
- The raw/processed data required to reproduce these findings cannot be shared at this time as the data also forms part of an ongoing study.

Declaration of Competing Interest

The authors declare that they have no known competing financial interests or personal relationships that could have appeared to influence the work reported in this paper.

Acknowledgements

We authors are deeply grateful to Dr. Maria Elisa Chuery Martins Rostelato from Radiation Technology Centre (CTR), Dr. Ivana Conte Cosentino from Science and Technology of Materials Centre (CCTM) both at Nuclear and Energy Research Institute (IPEN/CNEN-SP, Sao Paulo, Brazil). In addition to the following sponsor organizations: São Paulo Research Foundation (FAPESP), grant# 2022/06695-0; National Council for Scientific and Technological Development (CNPq); and Coordination for Improvement of High Degree People (CAPES).

References

[1] K. Ozasa, H.M. Cullings, W. Ohishi, A. Hida, E.J. Grant, Epidemiological studies of atomic bomb radiation at the Radiation Effects Research Foundation, Int. J. Radiat. Biol. 95 (2019) 879–891, https://doi.org/10.1080/09553002.2019.1569778.

[2] V. Chopra, Y.R. Parauha, D. Poelman, S.J. Dhoble, Chapter 2 - Principle, mechanism, and models of radiation dosimetry, in: S. Dhoble, V. Chopra, V. Nayar, G. Kitis, D. Poelman, H.B.T.-R.D.P. Swart (Eds.), Woodhead Publ. Ser. Electron. Opt. Mater., Woodhead Publishing, 2022, pp. 27–45, https://doi.org/10.1016/B978-0-323-85471-9.00012-9.

[3] S.N.M. Nawi, M.U. Khandaker, D.A. Bradley, S.F.A. Sani, K.S. Almugren, A. Sulieman, Polymer pencil lead graphite for in vivo radiation dosimetry, Diam. Relat. Mater. 106 (2020), 107860, https://doi.org/10.1016/j.diamond.2020.107860.

[4] K. Hoshi, H. Yoshitomi, K. Aoki, Y. Tanimura, N. Tsujimura, S. Yokoyama, Eye lens dosimetry for workers at Fukushima Daiichi Nuclear Power Plant—1: Laboratory study on the dosemeter position and the shielding effect of full face mask respirators, Radiat. Meas. 134 (2020), 106304, https://doi.org/10.1016/j.radmeas.2020.106304.

[5] N. Kataoka, D. Kawahara, M. Sekiguchi, Uniform irradiation of table eggs in the shell with low-energy electron beams, Radiat. Phys. Chem. 202 (2023), 110553, https://doi.org/10.1016/j.radphyschem.2022.110553.

[6] S. Gharazi, K.R. Mecadon, L. Gonzalez-Lopez, M. Al-Sheikhly, On the mechanism of radiation and thermal-induced degradation of the insulation cables in nuclear power plants-the presence of long-lived polyenyl C-centered radicals, Radiat. Phys. Chem. 203 (2023), 110603, https://doi.org/10.1016/j.radphyschem.2022.110603.

[7] X.M. He, S.G. Swarts, E. Demidenko, A.B. Flood, O. Grinberg, J. Gui, M. Mariani, S. D. Marsh, A.E. Ruuge, J.W. Sidabras, D. Tipikin, D.E. Wilcox, H.M. Swartz, Development and validation of an ex vivo electron paramagnetic resonance fingernail biodosimetric method, Radiat. Prot. Dosimetry. 159 (2014) 172–181, https://doi.org/10.1093/rpd/ncu129.

[8] S.C. Santos, L.L. Campos, Advances in colloidal processing of rare earth particles, Curr. Smart Mater. 3 (2018) 3–20, https://doi.org/10.2174/2405465802666171012143956.

[9] S. Santos, O. Rodrigues, L. Campos, A glance on rare earth oxides : importance, reserves, demand, applications, critical uncertainties, Global Econ. Zeta Potential Characterization (2020) 1–22, https://doi.org/10.2174/2405465805999200628095450.

[10] L. Mariscal-Becerra, V.M. Velázquez-Aguilar, M.C. Flores-Jiménez, J. M. Hernández-Álcantara, E. Camarillo-García, C.J. Villagómez, R. Váquez-Arreguín, I. Martínez-Merlin, C. Falcony-Guajardo, H. Murrieta, Up-conversion luminescence of hafnium, erbium, ytterbium and lithium co-doped yttrium oxide, Opt. Mater. (Amst). 105 (2020), 109923, https://doi.org/10.1016/j.optmat.2020.109923.

[11] T. Verma, S. Agrawal, Optical studies and estimation of kinetic parameters for dysprosium activated yttrium oxide phosphors, Optik (Stuttg) 160 (2018) 361–370, https://doi.org/10.1016/j.ijleo.2018.02.015.

[12] M.H. Shaaban, A.A. Ali, Density, electrical and optical properties of yttrium-containing tellurium bismuth borate glasses, J. Electron. Mater. 43 (2014) 4023–4032, https://doi.org/10.1007/s11664-014-3331-y.

[13] A. Kruk, A. Wajler, M. Bobruk, A. Adamczyk, M. Mrózek, W. Gawlik, T. Brylewski, Preparation of yttria powders co-doped with Nd3+, and La3+ using EDTA gel processes for application in transparent ceramics, J. Eur. Ceram. Soc. 37 (2017) 4129–4140, https://doi.org/10.1016/j.jeurceramsoc.2017.05.040.

[14] D. Yin, J. Wang, P. Liu, D. Luo, L.B. Kong, Z. Dong, D. Tang, Yttria nanopowders with low degree of aggregation by a spray precipitation method, Ceram. Int. 44 (2018) 20472–20477, https://doi.org/10.1016/j.ceramint.2018.08.042.

[15] N.J. Shivaramu, B.N. Lakshminarasappa, K.R. Nagabhushana, F. Singh, Synthesis characterization and luminescence studies of gamma irradiated nanocrystalline yttrium oxide, Spectrochim, Acta Part a-Molecular Biomol. Spectrosc. 154 (2016) 220–231, https://doi.org/10.1016/j.saa.2015.09.019.

[16] Y. Kim, J. Kim, J.-W. Han, J. Choi, Multiscale mechanics of yttria film formation during plasma spray coating, Appl. Surf. Sci. 572 (2022), 151416, https://doi.org/10.1016/j.apsusc.2021.151416.

[17] B. Baruah, R. Sarkar, Effect of Y2O3 content on densification, microstructure and mechanical properties of reaction sintered magnesium aluminate spinel, Ceram. Int. 49 (2023) 755–765, https://doi.org/10.1016/j.ceramint.2022.09.047.

[18] R. Patel, A.H. Fakeeha, S.O. Kasim, M.L. Sofiu, A.A. Ibrahim, A.E. Abasaeed, R. Kumar, A.S. Al-Fatesh, Optimizing yttria-zirconia proportions in Ni supported catalyst system for H2 production through dry reforming of methane, Mol. Catal. 510 (2021), 111676, https://doi.org/10.1016/j.mcat.2021.111676.

[19] L.R.R. Nunes, H.P. Labaki, F.J. Caixeta, R.R. Gonçalves, Yb3+ influence on NIR emission from Pr3+-doped spherical yttria nanoparticles for advances in NIR I and NIR II biological windows, J. Lumin. 241 (2022), 118485, https://doi.org/10.1016/j.jlumin.2021.118485.

[20] H. Reveron, J. Chevalier, Yttria-Stabilized Zirconia as a Biomaterial: From Orthopedic Towards Dental Applications, in: M.B.T.-E. of M.T.C. and G. Pomeroy (Ed.), Elsevier, Oxford, 2021: pp. 540–552. doi:10.1016/B978-0-12-818542-1.00030-8.

[21] N. Putenpurayil Govindan, A. Najafzadehkhoee, A. Talimian, V. Pouchly, M. Michálková, P. Švančárek, R. Klement, D. Galusek, Sintering of Ce3+-doped yttria nanoparticles prepared by precipitation method, Open Ceram 13 (2023), 100315, https://doi.org/10.1016/j.oceram.2022.100315.

[22] N.L. Wang, X.Y. Zhang, Z.H. Bai, Synthesis of neodymium doped yttria nanopowders by microwave-assisted glycine combustion method and the powder characteristics, Ceram. Int. 40 (2014) 4903–4908, https://doi.org/10.1016/j.ceramint.2013.10.073.

[23] Y. Huang, D. Jiang, J. Zhang, Q. Lin, Precipitation synthesis and sintering of lanthanum doped yttria transparent ceramics, Opt. Mater. (Amst). 31 (2009) 1448–1453, https://doi.org/10.1016/j.optmat.2009.01.015.

[24] C. Karunakaran, M. Balamurugan, Chapter Four - Electron Paramagnetic Resonance Spectroscopy, in: C.B.T.-S.R.S. Karunakaran (Ed.), Elsevier, 2018: pp. 169–228. doi:10.1016/B978-0-12-813608-9.00004-6.

[25] M. Boiani, C. Pacheco, Nuclear Magnetic Resonance, in: P.L.H. McSweeney, J.P.B. T.-E. of D.S. (Third E. McNamara (Eds.), Academic Press, Oxford, 2022: pp. 490–496. doi:10.1016/B978-0-12-818766-1.00168-9.

[26] M.J. Davies, Detection and characterisation of radicals using electron paramagnetic resonance (EPR) spin trapping and related methods, Methods 109 (2016) 21–30, https://doi.org/10.1016/j.ymeth.2016.05.013.

[27] L. Emmanouilidis, L. Esteban-Hofer, G. Jeschke, F.H.-T. Allain, Structural biology of RNA-binding proteins in the context of phase separation: What NMR and EPR can bring? Curr. Opin. Struct. Biol. 70 (2021) 132–138, https://doi.org/10.1016/j.sbi.2021.07.001.

[28] R. Romanet, Z. Sarhane, F. Bahut, J. Uhl, P. Schmitt-Kopplin, M. Nikolantonaki, R. D. Gougeon, Exploring the chemical space of white wine antioxidant capacity: ssa combined DPPH, EPR and FT-ICR-MS study, Food Chem 355 (2021), 129566, https://doi.org/10.1016/j.foodchem.2021.129566.

[29] R. Calvo, R.P. Sartoris, O.R. Nascimento, M. Šedivý, A. Sojka, P. Neugebauer, V. T. Santana, Quantum phase transitions probed by EPR spectra in dimeric spin arrays with supramolecular couplings, Coord. Chem. Rev. 480 (2023), 215007, https://doi.org/10.1016/j.ccr.2022.215007.

[30] J. Guo, L. Ma, X. Bi, G. Dong, Y. Li, J. Ning, K. Wu, X-band TE101 rectangular aperture cavity for in vivo EPR tooth dosimetry after radiation emergency, Appl. Radiat. Isot. 178 (2021), 109958, https://doi.org/10.1016/j.apradiso.2021.109958.

[31] A. Simion, S. Simon, C. Filip, M. Mureşan-Pop, A. Vulpoi, D.M. Petrişor, G. Damian, M. Vasilescu, M. Todea, Local structural effects of Gd3+ ions incorporation in shell of nanostructured silica core – alumina rich shell microspheres, J. Mol. Struct. 1284 (2023), 135381, https://doi.org/10.1016/j.molstruc.2023.135381.

[32] S.C. Santos, O. Rodrigues, L.L. Campos, EPR dosimetry of yttria micro rods, J. Alloys Compd. (2018), https://doi.org/10.1016/j.jallcom.2018.01.315.

[33] S.C. Santos, O. Rodrigues, L.L. Campos, EPR response of yttria micro rods activated by europium, J. Alloys Compd. (2018), https://doi.org/10.1016/j.jallcom.2018.06.063.

[34] S. C. L.L. Santos, O. Rodrigues Jr, Campos, Formation and EPR response of europium yttria micro rods, Brazilian Electron J. Physics, Chem. Mater. Sci. 1 (2019) 6, https://doi.org/10.34019/2674-9688.2019.v1.28229.

[35] S.C. Santos, O. Rodrigues, L.L. Campos, Bio-prototyping of europium-yttria based rods for radiation dosimetry, Mater. Chem. Phys. (2017), https://doi.org/10.1016/j.matchemphys.2017.07.063.

[36] S.C. Santos, O. Rodrigues, L.L. Campos, Radiation effects on microstructure and EPR signal of yttrium oxide rods, IOP Conf. Ser. Mater. Sci. Eng. 169 (2017), 012009, https://doi.org/10.1088/1757-899X/169/1/012009.

[37] S.C. Santos, O. Rodrigues, L.. Campos, Dispersion of thulium-yttria nanoparticles to build up smart structures, Mater. Today Commun. (2020), 101749, https://doi.org/10.1016/j.mtcomm.2020.101749.

[38] S.C. Santos, O. Rodrigues, L.L. Campos, Towards a new promising dosimetric material from formation of thulium-yttria nanoparticles with EPR response, Mater. Chem. Phys. 259 (2021), 124005, https://doi.org/10.1016/j.matchemphys.2020.124005.

[39] S.C. Santos, O. Rodrigues, L.L. Campos, Colloidal processing of thulium-yttria microceramics, J. Phys. Chem. Solids. 161 (2022), 110420, https://doi.org/10.1016/j.jpcs.2021.110420.

[40] R. Saravanan, Y. Ono, M. Isshiki, K. Ohno, T. Kajitani, Electron density distribution in GaAs using MEM, J. Phys. Chem. Solids. 64 (2003) 51–58, https://doi.org/10.1016/S0022-3697(02)00209-3.

[41] N. Doebelin, R. Kleeberg, Profex: a graphical user interface for the Rietveld refinement program, J. Appl. Crystallogr. 48 (2015) 1573–1580, https://doi.org/10.1107/S1600576715014685.

[42] K. Momma, F. Izumi, VESTA: a three-dimensional visualization of crystal, volumetric and morphology data, J. Appl. Crystallogr. 44 (2011) 1272–1276, https://doi.org/10.1107/S0021889811038970.

[43] D. Melcher, Contributions to grain/sub-grain size analysis using X-ray powder diffractometry, TU Dresden, 1988.

[44] J. Bergmann, Rietveld Analysis Program BGMN, (2005) 130. http://www.bgmn.de/BGMN_manual_2005.pdf.

[45] W. Tscharnuter, Photon Correlation Spectroscopy in Particle Sizing, 1st ed., John Wiley & Sons Ltd, United States of America, 2000. http://www.brookhaveninstruments.com/literature/lit_90Plus.html.

[46] P. A. Paul, C. Webb, Analytical methods in fine particle technology, Orr, Micromeritics Instrument Corporation, Norcross, Ga, 1997.

[47] P.O. Theillet, O.N. Pierron, Quantifying adsorbed water monolayers on silicon MEMS resonators exposed to humid environments, Sens. Actuators A-Physical 171 (2011) 375–380.

[48] R. Tlili, M. Bejar, E. Dhahri, A. Zaoui, E.K. Hlil, L. Bessais, Influence of crystallite size reduction on the magnetic and magnetocaloric properties of La0.6Sr0.35Ca0.05CoO3 nanoparticles, Polyhedron 121 (2017) 19–24, https://doi.org/10.1016/j.poly.2016.09.044.

[49] B. Zhang, F. Wang, J. Chen, B. Li, X. Shen, K. Liu, Q. Han, Preparation of silicon crystallites via controllable thermal reduction of amorphous silica, Mater. Lett. 316 (2022), 131996, https://doi.org/10.1016/j.matlet.2022.131996.

[50] J.P. Coutures, R. Verges, M. Foex, Comparison of solidification temperatures of different rare earth sesquioxides; effect of atmosphere, Rev. Int. Des Hautes Temp. Des Refract. 12 (1975) 181–185. http://inis.iaea.org/search/search.aspx?orig_q=RN:07227877.

[51] K. Riener, N. Albrecht, S. Ziegelmeier, R. Ramakrishnan, L. Haferkamp, A. B. Spierings, G.J. Leichtfried, Influence of particle size distribution and morphology on the properties of the powder feedstock as well as of AlSi10Mg parts produced by laser powder bed fusion (LPBF), Addit. Manuf. 34 (2020), 101286, https://doi.org/10.1016/j.addma.2020.101286.

[52] X. Qin, Y. Ju, S. Bernhard, N. Yao, Flame synthesis of Y 2 O 3 :Eu nanophosphors using ethanol as precursor solvents, J. Mater. Res. 20 (2005) 2960–2968, https://doi.org/10.1557/JMR.2005.0364.

[53] H. Starr, Territory, proximity, and spatiality: the geography of international conflict, Int. Stud. Rev. 7 (2005) 387–406, https://doi.org/10.1111/j.1551-2916.2005.00506.x.

[54] R. Zamiri, H. Mahmoudi Chenari, H.F. Moafi, M. Shabani, S.A. Salehizadeh, A. Rebelo, J.S. Kumar, M.P.F. Graça, M.J. Soares, J.M.F. Ferreira, Ba-doped ZnO nanostructure: X-ray line analysis and optical properties in visible and low frequency infrared, Ceram. Int. 42 (2016) 12860–12867, https://doi.org/10.1016/j.ceramint.2016.05.051.

[55] K. Park, H.K. Hwang, J.W. Seo, W.-S. Seo, Enhanced high-temperature thermoelectric properties of Ce- and Dy-doped ZnO for power generation, Energy 54 (2013) 139–145, https://doi.org/10.1016/j.energy.2013.03.023.

[56] S. Suwanboon, P. Amornpitoksuk, A. Sukolrat, N. Muensit, Optical and photocatalytic properties of La-doped ZnO nanoparticles prepared via precipitation

and mechanical milling method, Ceram. Int. 39 (2013) 2811–2819, https://doi.org/10.1016/j.ceramint.2012.09.050.
[57] M. El-Kinawy, F. Abdel-Wahab, N. Seriani, N. El-Faramawy, DFT study of the role of point and complex defects on luminescence, electronic, and thermodynamic properties of LiF: Mg, Mater. Res. Bull. 158 (2023), 112044, https://doi.org/10.1016/j.materresbull.2022.112044.
[58] Y. Guo, C. Chen, Q. Wang, Y. Cao, C. Wu, K. Zhou, Microstructural evolution and mechanical behavior of additively manufactured tantalum produced by electron beam powder bed fusion, Int. J. Refract. Met. Hard Mater. 110 (2023), 106046, https://doi.org/10.1016/j.ijrmhm.2022.106046.
[59] S. Jiang, C. Liu, P. Liu, H. Yin, G.-P. Zheng, Electron-doping induced tunable magnetisms in 2D Janus TiXO (X = S, Se), Phys. E Low-Dimensional Syst. Nanostructures 145 (2023), 115518, https://doi.org/10.1016/j.physe.2022.115518.
[60] X. Jin, H. Guan, R. Wang, L. Huang, C. Shao, The most crucial factor on the thermal conductivity of metal-water nanofluids: Match degree of the phonon density of state, Powder Technol 412 (2022), 117969, https://doi.org/10.1016/j.powtec.2022.117969.
[61] J. Plévert, T.J. White, Structure Types and Classifications, in: F. Bassani, G.L. Liedl, P.B.T.-E. of C.M.P. Wyder (Eds.), Elsevier, Oxford, 2005: pp. 54–60. doi:10.1016/B0-12-369401-9/00687-2.
[62] Y. Liu, L. Zhan, L. Wen, L. Cheng, Y. He, B. Xu, Q. Wu, S. Liu, Effects of particle size and color on photocuring performance of Si3N4 ceramic slurry by stereolithography, J. Eur. Ceram. Soc. 41 (2021) 2386–2394, https://doi.org/10.1016/j.jeurceramsoc.2020.11.032.
[63] D. Pu, X. Chen, Y. Ding, Y. Sun, B. Feng, K. Zheng, F. Pan, Effect of Ti particles size on the microstructure and mechanical properties of TiP/VW94 composites, Mater. Sci. Eng. A. 858 (2022), 144140, https://doi.org/10.1016/j.msea.2022.144140.
[64] S. Chen, C.-S. Wang, W. Zheng, J.-M. Wu, C.-Z. Yan, Y.-S. Shi, Effects of particle size distribution and sintering temperature on properties of alumina mold material prepared by stereolithography, Ceram. Int. 48 (2022) 6069–6077, https://doi.org/10.1016/j.ceramint.2021.11.145.
[65] R. Han, N. ul H. Tariq, H. Liu, L. Zhao, J. Luo, J. Wang, X. Cui, T. Xiong, Development of high infrared emissivity porous ceramic coating using pre-synthesized flower-like CeO2 powder for high temperature applications, Ceram. Int. 48 (2022) 1340–1348, https://doi.org/10.1016/j.ceramint.2021.09.218.
[66] Z.-M. Dong, Q. Xia, H. Ren, X. Shang, X. Lu, S.W. Joo, J. Huang, Preparation of hollow SnO2/ZnO cubes for the high-performance detection of VOCs, Ceram. Int. (2022), https://doi.org/10.1016/j.ceramint.2022.09.352.
[67] X. Yu, Z. Han, H. Tang, J. Xie, X. Mi, Investigating luminescence properties and energy transfer of Ca3(PO4)2: Dy3+/Eu3+ phosphor via hydrothermal synthesis, Opt. Mater. (Amst). 106 (2020), 110009, https://doi.org/10.1016/j.optmat.2020.110009.
[68] B. Arul Prakasam, M. Lahtinen, A. Peuronen, M. Muruganandham, M. Sillanpää, Facile fabrication of flower like self-assembled mesoporous hierarchical microarchitectures of In(OH)3 and In2O3: In(OH)3 micro flowers with electron beam sensitive thin petals, Mater. Chem. Phys. 184 (2016) 183–188, https://doi.org/10.1016/j.matchemphys.2016.09.040.
[69] J.H. Lunsford, Esr of adsorbed oxygen species, Catal. Rev. Eng. 8 (1973) 135–157.
[70] Y. Osada, S. Koike, T. Fukushima, S. Ogasawara, T. Shikada, T. Ikariya, Oxidative coupling of methane over Y2o3-Cao catalysts, Appl. Catal. 59 (1990) 59–74, https://doi.org/10.1016/S0166-9834(00)82187-9. Doi.
[71] K. Singh, V. Thangadurai, Chemical reactivity between Ce0.7RE0.2Mo0.1O2 (RE = Y, Sm) and 8YSZ, and conductivity studies of their solid solutions, Solid State Ionics 262 (2014) 444–448, https://doi.org/10.1016/j.ssi.2014.03.030.
[72] O.M. Bordun, Influence of oxygen vacancies on the luminescence spectra of Y2O3 thin films, J. Appl. Spectrosc. 69 (2002) 430–433, https://doi.org/10.1023/a:1019763518857.